An effective finite-element-based method for the computation of nonlinear normal modes of nonconservative systems

L. Renson[1], G. Deliége[2], G. Kerschen[1]

[1]Space Structures and Systems Laboratory,
Department of Aerospace and Mechanical Engineering,
University of Liège, Liège, Belgium.
[2] Computational Nonlinear Mechanics,
Department of Aerospace and Mechanical Engineering,
University of Liège, Liège, Belgium.

Corresponding author: L. Renson
Email: l.renson@ulg.ac.be, phone: +32 4 3664854.

Abstract

This paper addresses the numerical computation of nonlinear normal modes defined as two-dimensional invariant manifolds in phase space. A novel finite-element-based algorithm, combining the streamline upwind Petrov-Galerkin method with mesh moving and domain prediction-correction techniques, is proposed to solve the manifold-governing partial differential equations. It is first validated using conservative examples through the comparison with a reference solution given by numerical continuation. The algorithm is then demonstrated on nonconservative examples.

keywords: Nonlinear normal modes, Invariant manifolds, Nonconservative systems, Modal analysis, Finite element method

1 Introduction

The dynamic systems theory is well-established for linear systems and can rely on mature tools such as the theories of linear operators and linear integral transforms. This is why modal analysis, i.e., the computation of vibration modes, is really quite sophisticated and advanced. Even though linear modal analysis served, and is still serving, the structural dynamics community for applications ranging from bridges to satellites, it is commonly accepted that nonlinearity is a frequent occurrence in engineering structures. Because linear modal analysis fails to provide an accurate description of nonlinear dynamical phenomena, the development of a practical nonlinear analog of modal analysis is a problem of great timeliness and importance.

Pioneered in the 1960s by Rosenberg [1], nonlinear normal modes (NNMs) are a rigorous extension of linear normal modes (LNMs) to nonlinear systems. The concept was then

further developed [2, 3] and enjoyed various applications in nonlinear structural dynamics, see, e.g., [4, 5, 6, 7, 8, 9]. First defined as families of *vibration in unison* of the undamped, unforced system [1], NNMs were latter defined as (non-necessarily synchronous) periodic oscillations in order to account for modal interactions [10, 11]. Considering NNMs as periodic oscillations of autonomous nonlinear systems is appealing, because they can be effectively computed using algorithms for the numerical continuation of periodic orbits [12, 13]. This paves the way for application of the NNM concept to real-life structures [14].

If the damped dynamics of a nonlinear system can often be interpreted based on the topological structure and bifurcations of the NNMs of the underlying Hamiltonian system, "simple" viscous damping may sometimes drastically alter the dynamics, e.g., by turning hardening nonlinear behavior into softening behavior [15]. In addition, complex, nonlinear damping mechanisms are present in virtually all engineering applications. In the 1990s, Shaw and Pierre proposed an alternative definition that provides an elegant extension of NNMs to damped systems. Based on geometric arguments and inspired by the center manifold theory, they defined an NNM as a two-dimensional invariant manifold in phase space [3]. The approach was demonstrated on continuous systems [16] and piecewise-linear systems [17]. It was extended to forced systems [18] and multi-modal NNMs [19].

The first attempt to carry out numerical computation of NNMs as invariant manifolds is that of Pesheck et al. [20]. The manifold-governing partial differential equations (PDEs) were written in modal space using polar coordinates and solved using a Galerkin projection. Eventually, a set of highly-coupled and highly-nonlinear algebraic equations were to be solved. Although the method is computationally demanding [21], it clearly eliminates a number of problems associated with the local polynomial approximation of the manifold [3]. It was generalized to consider piecewise-linear nonlinearities [22], forced systems [23], and multi-modal NNMs [24, 25], but there were few applications of the method to damped systems [26]. In a recent contribution, Touzé and co-workers [27] also solved the PDEs in modal space numerically. They recognized that the PDEs can be written in terms of transport equations, which, in turn, allows to discretize them using finite differences. This method was shown to accurately compute invariant manifolds of conservative systems, but it is seemingly not yet applicable to nonconservative systems [27]. Another interesting work uses a Fourier-Galerkin expansion procedure to solve a nonlinear eigenvalue problem with NNMs defined in terms of frequency and modal vectors, both functions of amplitude and phase. First established for conservative systems [28], the method was then extended to nonconservative systems [29]. In [30], the concept of complex nonlinear modes is introduced, and a nonlinear complex eigenproblem is derived based on a definition of eigenfunctions as generalized Fourier series.

The present paper proposes a new, effective method for the computation of NNMs defined as two-dimensional invariant manifolds in phase space. A specific finite-element-based (FE-based) strategy is developed to address two important challenges, namely the hyperbolic nature of the manifold-governing PDEs and the computational burden associated with applications possessing more than a few degrees of freedom.

The paper is organized as follows. NNMs defined as invariant manifolds are briefly re-

viewed in Section 2. The interpretation of the manifold-governing PDEs in terms of flow equations encountered in fluid dynamics is also presented. Section 3 introduces the specific FE-based strategy for computing invariant manifolds of conservative systems. In Section 4, the method is validated against algorithms for numerical continuation of periodic orbits using two conservative examples, namely a two-degree-of-freedom (2DOF) system including quadratic and cubic nonlinearities and a cantilever beam with nonlinear boundary conditions. In Section 5, the proposed algorithm is extended to nonconservative systems and demonstrated using the same 2DOF and beam examples. The conclusions of the present study are summarized in Section 6.

2 Nonlinear normal modes as invariant manifolds in phase space

A detailed description of NNMs and of their fundamental properties (e.g., frequency-energy dependence, bifurcations, and stability) is given in [2, 11] and is beyond the scope of this paper. In the present contribution, the free response of discrete mechanical systems with N degrees of freedom (DOFs) is considered, assuming that continuous systems have been spatially discretized. The ordinary differential equations of motion are

$$\mathbf{M}\,\ddot{\mathbf{x}}(t) + \mathbf{C}\,\dot{\mathbf{x}}(t) + \mathbf{K}\,\mathbf{x}(t) + \mathbf{f}_{\text{nl}}\left(\mathbf{x}(t), \dot{\mathbf{x}}(t)\right) = 0 \tag{1}$$

where $\mathbf{M}$, $\mathbf{C}$, and $\mathbf{K}$ are the mass, damping, and stiffness matrices, respectively; $\mathbf{x}$, $\dot{\mathbf{x}}$, and $\ddot{\mathbf{x}}$ are the displacement, velocity, and acceleration vectors, respectively; $\mathbf{f}_{\text{nl}}$ is the nonlinear restoring force vector. The system of equation (1) is transformed into its first-order form

$$\begin{aligned} \dot{\mathbf{x}} &= \mathbf{y}, \\ \dot{\mathbf{y}} &= \mathbf{f} \quad = -\mathbf{M}^{-1}\left(\mathbf{C}\,\dot{\mathbf{x}} + \mathbf{K}\,\mathbf{x} + \mathbf{f}_{\text{nl}}\left(\mathbf{x}, \dot{\mathbf{x}}\right)\right) \end{aligned} \tag{2}$$

where the term $\mathbf{f}$ represents all the inertia-normalized (linear and nonlinear) elastic and dissipative forces in the equations of motion.

Shaw and Pierre defined an NNM as a two-dimensional invariant manifold in phase space [3]. The manifold is parametrized using a single pair of state variables, i.e., a displacement x_k and a velocity y_k, chosen as master coordinates (u, v). The remaining variables are functionally related to the chosen pair through

$$\begin{aligned} x_i &= X_i(u, v), \\ y_i &= Y_i(u, v), \qquad i = 1, ..., N;\ i \neq k. \end{aligned} \tag{3}$$

The elimination of the time dependence in the equations leads to a set of 2N-2 partial

differential equations (PDEs) that can be solved for the X_i's and Y_i's

$$\begin{aligned} Y_i(u,v) &= \frac{\partial X_i(u,v)}{\partial u} v + \frac{\partial X_i(u,v)}{\partial v} f_k, \\ f_i &= \frac{\partial Y_i(u,v)}{\partial u} v + \frac{\partial Y_i(u,v)}{\partial v} f_k, \\ \text{where } i &= 1,...,N;\ i \neq k, \\ f_i &= f_i(u, \mathbf{X}(u,v), v, \mathbf{Y}(u,v)) \\ \text{and } \mathbf{X} &= \{X_j : j = 1,...,N\ ; j \neq k\} \\ \mathbf{Y} &= \{Y_j : j = 1,...,N\ ; j \neq k\} \end{aligned} \tag{4}$$

The f_is are the components of $\mathbf{f}$ (cf. Equation (2)).

Around the system's equilibrium point, the manifold governing PDEs (4) admit N solutions which are the extension of the N underlying LNMs [3]. At the origin, each NNM is tangent to the linear eigenspace spanned by the corresponding LNM. Once they are solved, the constraint equations (3) provide a geometric description of the NNMs in phase space. They correspond to two-dimensional surfaces that are tangent to the corresponding LNMs at the equilibrium point. The single-DOF motion on the nonlinear mode of interest is generated by substituting the X_i's and Y_i's in the equations of motion governing the master coordinates x_k and y_k:

$$\begin{aligned} \dot{u} &= v, \\ \dot{v} &= f_k(u, \mathbf{X}(u,v), v, \mathbf{Y}(u,v)). \end{aligned} \tag{5}$$

Interestingly, Equations (4) can be recast into

$$\begin{cases} \mathbf{V} \cdot \nabla X_i - Y_i = 0, & \mathbf{V}^T = \{v \ \ f_k\} \\ \mathbf{V} \cdot \nabla Y_i - f_i = 0, & i = 1,...,N;\ i \neq k. \end{cases} \tag{6}$$

where ∇ stands for the gradient operator. These equations are quasilinear first-order hyperbolic PDEs that bear a resemblance to flow equations encountered in fluid dynamics. The flow corresponds to the system dynamics projected onto the (u, v) plane, and $\mathbf{V}$ may be read as the velocity vector of the flow. This interpretation is identical to the interpretation of the PDEs as a transport problem [27].

Figure 1 shows the flow of the 2DOF nonlinear conservative system considered in Section 4.1. The flow $\mathbf{V}$ was obtained after solving the manifold governing PDEs using the proposed method. It is everywhere tangent to characteristic curves (or characteristics) that illustrate the propagation of the "information" into the domain. In the conservative context, the characteristics coincide with the closed iso-energy curves of the system, i.e., the isolated periodic solutions of the NNM. The reader should refer to references [31, 32] for further details about hyperbolic PDEs.

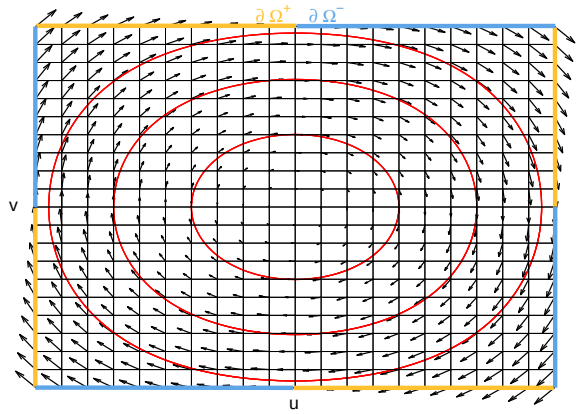

Figure 1: Flow $\mathbf{V}$ of the manifold-governing PDEs for the 2DOF nonlinear conservative system considered in Section 4.1 and for a finite domain Ω. The velocity field ($\rightarrow$) is tangent to iso-energy curves (–). The inflow and outflow boundaries, $\partial\Omega^-$ and $\partial\Omega^+$, are underlined in blue and orange, respectively.

3 Computation of nonlinear normal modes using the finite element method

This section presents a rigorous and effective methodology for the computation of NNMs that exploits the interpretation of the PDEs as fluid flow equations. The conservative case is considered in this section, whereas the computational method is extended to non-conservative systems in Section 5.

Targeting a solution for finite amplitudes, the PDEs are solved in a finite domain Ω whose boundary is denoted $\partial\Omega$. As illustrated in Figure 1, this boundary may comprise inflow and outflow regions

$$\begin{aligned} \partial\Omega^- &: \{\mathbf{u} = (u, v) \in \Omega : \mathbf{V}(\mathbf{u}).\mathbf{n}(\mathbf{u}) < 0\} \\ \partial\Omega^+ &: \{\mathbf{u} = (u, v) \in \Omega : \mathbf{V}(\mathbf{u}).\mathbf{n}(\mathbf{u}) > 0\}, \end{aligned} \tag{7}$$

respectively. $\mathbf{n}(\mathbf{u})$ is the outward normal vector to $\partial\Omega$.

Solving hyperbolic PDEs requires boundary conditions (BCs) at inflow where the velocity vector $\mathbf{V}$ points inward the domain. Indeed, even if there are no BCs in Equations (6), the solution along the incoming characteristic depends mathematically on the solution outside the domain. This is why the unknown field values (X_i, Y_i) have to be imposed on $\partial\Omega^-$. The mathematical problem to solve becomes

$$\begin{cases} \mathbf{V} \cdot \nabla X_i - Y_i = 0, & \\ \mathbf{V} \cdot \nabla Y_i - f_i = 0, & \mathbf{V}^T = \{v \;\; f_k\} \\ X_i|_{\partial\Omega^-} = X_i^-, & i = 1, ..., N;\; i \neq k, \\ Y_i|_{\partial\Omega^-} = Y_i^-, & \end{cases} \tag{8}$$

A difficulty is that BCs at $\partial\Omega^-$ cannot be set before the actual solution is known. One interesting observation in Figure 1 is that the flow is tangent to the iso-energy curves, i.e., there is no inflow if the computation domain coincides with an iso-energy curve. Indeed, on the one hand, based on Hamilton's principle, the power balance for a conservative system writes

$$\frac{d}{dt}\mathcal{E} = \frac{d}{dt}\left(\mathcal{K} + \mathcal{V}\right) = 0 \tag{9}$$

where $\mathcal{E}$, $\mathcal{K}$, and $\mathcal{V}$ are the total, kinetic, and potential energy, respectively. On the other hand, $\mathcal{E} = \mathcal{E}(\mathbf{u})$ on the invariant manifold describing the NNM. This leads to

$$\frac{d}{dt}\mathcal{E}(\mathbf{u}) = \nabla\mathcal{E}.\frac{d\mathbf{u}}{dt} = \nabla\mathcal{E}.\mathbf{V}. \tag{10}$$

This last expression equals zero if and only if the flow is locally everywhere tangent to the iso-energy curve defined by $\mathcal{E}$. In this case, no BCs have to be imposed. In addition, two iso-energy curves form the inner and outer boundaries of an annular domain in which no inflow exists. The invariant manifold can therefore be computed considering subsequent annular domains, which substantially reduces the computational burden.

The computational method proposed herein exploits this strategy and is represented schematically in Figure 2. It starts in a small domain centered around the origin in which the system is assumed to behave linearly. A first guess of the iso-energy curve that realizes the domain boundary is obtained based on the corresponding LNM. To compute the invariant manifold in this domain, the boundary is first corrected to better fit the actual iso-energy curve. This is carried out thanks to a mesh-moving technique discussed in Section 3.1. Then, an iteration of a specific FE method described in Section 3.2 is performed. The mesh-moving and FE methods are applied sequentially until the solution is computed with a given accuracy. A new annular domain is predicted based on the computed solution, as presented in Section 3.3, and the PDEs are solved in this new computational domain following the same procedure. The algorithm is stopped after a user-defined number of regions (N_{max}), at a user-defined energy (E_{max}), or when the manifold parameterization fails (cf. discussion in Section 4.2). Eventually, the different annular domains are merged to form a single domain by defining a global mesh that interpolates over all the local meshes.

3.1 Domain correction using a mesh-moving technique

The first step of the algorithm corrects the assumed domain boundary to make it coincide with an iso-energy curve. To this end, the boundary is moved according to the energy difference $\Delta\mathcal{E}_n$ between a reference node and each other boundary node n. The reference node is defined as the boundary node with the smallest energy. As shown in Figure 2(b), this ensures that the corrected boundary is enclosed into the initial boundary so that delicate extrapolation between meshes is avoided.

The corrections $\mathbf{\Delta u}^n = [\Delta u^n \Delta v^n]^T$ to boundary node n are calculated by linearizing the

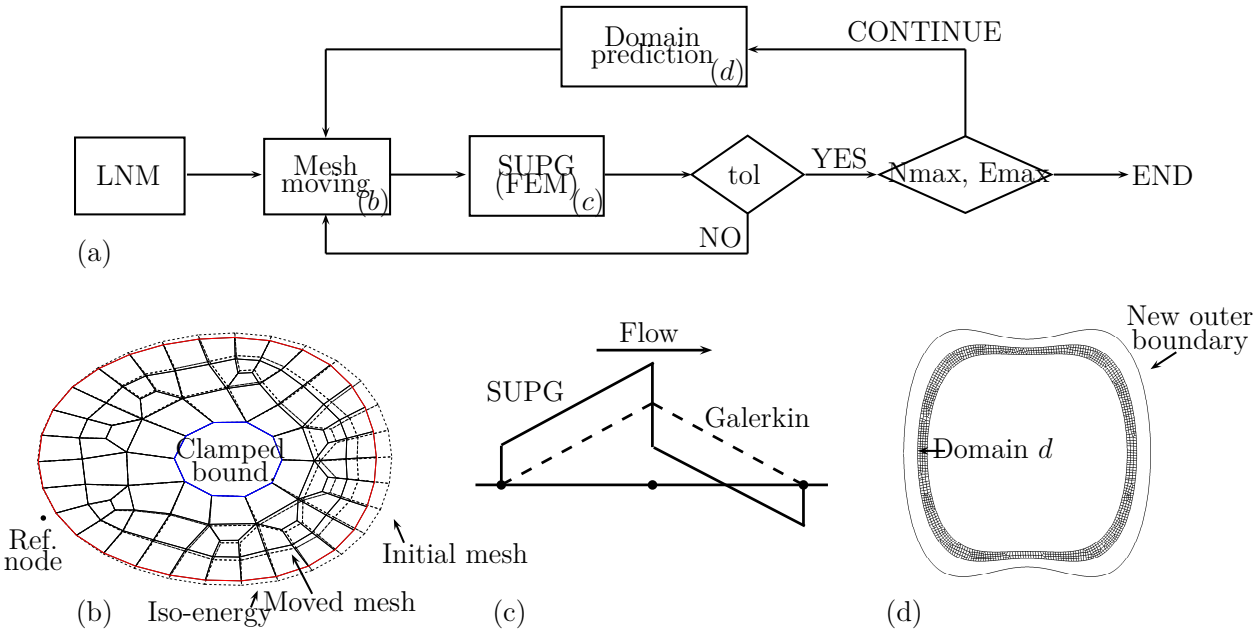

Figure 2: Schematics of the algorithm resolution strategy (a) including the mesh moving operation (b), the finite element formulation using SUPG (c), and the domain prediction (d).

energy around this node considering that u and v are independent

$$\Delta\mathcal{E}^n = \mathcal{E}^{\text{ref.}} - \mathcal{E}^n = \left.\frac{d\mathcal{E}}{du}\right|^n \Delta u^n + \left.\frac{d\mathcal{E}}{dv}\right|^n \Delta v^n. \tag{11}$$

The total derivatives of the energy with respect to the master coordinates are derived using the chain rule for differentiation

$$\begin{aligned} \frac{d\mathcal{E}^n}{du} &= \left.\frac{\partial\mathcal{E}}{\partial u}\right|^n + \left.\frac{\partial\mathcal{E}}{\partial\mathbf{X}}\right|^n \left.\frac{\partial\mathbf{X}}{\partial u}\right|^n + \left.\frac{\partial\mathcal{E}}{\partial\mathbf{Y}}\right|^n \left.\frac{\partial\mathbf{Y}}{\partial u}\right|^n, \\ \frac{d\mathcal{E}^n}{dv} &= \left.\frac{\partial\mathcal{E}}{\partial v}\right|^n + \left.\frac{\partial\mathcal{E}}{\partial\mathbf{X}}\right|^n \left.\frac{\partial\mathbf{X}}{\partial v}\right|^n + \left.\frac{\partial\mathcal{E}}{\partial\mathbf{Y}}\right|^n \left.\frac{\partial\mathbf{Y}}{\partial v}\right|^n. \end{aligned} \tag{12}$$

The partial derivatives of the unknown fields $(\mathbf{X}, \mathbf{Y})$ with respect to (u, v) are obtained through finite element interpolation whereas the partial derivatives of the energy with respect to $(\mathbf{X}, \mathbf{Y})$ almost reduce to the equations of motion (1).

To preserve a well-shaped mesh during boundary corrections, the annular domain is viewed as a pseudo-elastic medium for which the nodes follow the solution of an in-plane linear elasticity problem [33, 34]. This is illustrated in Figure 2(b). The main advantage of mesh-moving techniques is that remeshing operations are not necessary, which decreases the computational cost.

The equations governing the nodal displacements $\mathbf{\Delta u}$ are

$$\nabla.\sigma = \mathbf{0}, \quad \sigma = \mathbf{D} : \epsilon, \quad \epsilon = \frac{1}{2}(\nabla\mathbf{\Delta u} + \nabla\mathbf{\Delta u}^{\mathrm{T}}), \tag{13}$$

$$\mathbf{D}_{ijkl} = \frac{E\nu}{(1+\nu)(1-2\nu)}\delta_{ij}\delta_{kl} + \frac{E}{1+\nu}\left(\frac{1}{2}\delta_{ik}\delta_{jl} + \frac{1}{2}\delta_{il}\delta_{jk}\right). \tag{14}$$

The operator $\nabla.(.)$ denotes the divergence operator, σ the Cauchy stress tensor, $\mathbf{D}$ the Hooke tensor, ϵ the strain tensor, E the Young's modulus, ν the Poisson's ratio, and δ_{ij} the Kronecker delta. The parameter values are not critical and are set to $E = 10^8\ Pa$, $\nu = -0.25$ throughout this study. However, to preserve element aspect ratios, ν must be negative.

After discretization using the finite element method, a linear algebraic problem, $\mathbf{K}^{\text{elast}}\boldsymbol{\Delta}\mathbf{u} = \mathbf{0}$, is obtained where $\mathbf{K}^{\text{elast}}$ denotes the stiffness matrix of the discretized annular domain. The nodes are partitioned into three sets, namely clamped (inner), interior and outer nodes

$$\begin{bmatrix} \mathbf{K}_{cc} & \mathbf{K}_{ci} & \mathbf{K}_{co} \\ \mathbf{K}_{ic} & \mathbf{K}_{ii} & \mathbf{K}_{io} \\ \mathbf{K}_{oc} & \mathbf{K}_{oi} & \mathbf{K}_{oo} \end{bmatrix}^{\text{elast}} \begin{bmatrix} \boldsymbol{\Delta}\mathbf{u}_c \\ \boldsymbol{\Delta}\mathbf{u}_i \\ \boldsymbol{\Delta}\mathbf{u}_o \end{bmatrix} = \mathbf{0} \tag{15}$$

The inner nodes are clamped (i.e., $\boldsymbol{\Delta}\mathbf{u}_c = \mathbf{0}$), and the outer nodes follow the corrections computed through Equations (11). The displacements of the interior nodes are then computed through

$$\boldsymbol{\Delta}\mathbf{u}_i = -\mathbf{K}_{ii}^{-1}\mathbf{K}_{io}\boldsymbol{\Delta}\mathbf{u}_o \tag{16}$$

Domain corrections are recursively applied until the mean and standard deviation of the energy difference of all outer-boundary nodes are below a certain tolerance.

3.2 Streamline Upwind Petrov-Galerkin (SUPG)

Standard Galerkin FE formulations use identical shape and test functions. They are known to exhibit poor performance in the case of first-order hyperbolic PDEs, such as those encountered in fluid dynamics [35, 36, 37]. Specifically, a suboptimal convergence rate as well as spurious oscillations in the solutions were observed. As a remedy, numerous stabilization methods, based on alternative test functions, were introduced. Among the many techniques introduced, the streamline upwind Petrov-Galerkin (SUPG) method proved to be effective and is considered herein. It falls within the family of Petrov-Galerkin formulations where test and shape functions are taken in different spaces and overweights test functions that are upstream. The approach is rather standard in computational mechanics, and the interested reader can refer to [37] for a detailed description of SUPG method.

Applying a weighted residual approach to Equations (6) where the variations $\delta\tilde{Y}_i$ and $\delta\tilde{X}_i$ are applied to preserve consistent units yields

$$\int_\Omega \left[\mathbf{V}\cdot\nabla X_i(u,v) - Y_i(u,v)\right]\delta\tilde{Y}_i\, d\Omega = 0 \tag{17}$$

$$\int_\Omega \left[\mathbf{V}\cdot\nabla Y_i(u,v) - f_i(u,v,\mathbf{X},\mathbf{Y})\right]\delta\tilde{X}_i\, d\Omega = 0 \tag{18}$$

with $i = 1, ..., N \neq k$. The shape functions are first-order Lagrange shape functions, $N^b \in \mathbb{P}^1$. The test functions are $\tilde{N}^b = N^b + \tau \mathbf{V}.\nabla N^b$ where $\tau \mathbf{V}.\nabla N^b$ is the upstream overweighting. As a consequence, discontinuous test functions are employed, as illustrated in Figure 2(c) [38]. In fluid dynamics, parameter τ is defined based on the Peclet number, which is a measure of the ratio between convection and diffusion in a flow. In the present study, taking the limit for pure convection, $\tau = \frac{h^e}{2||\mathbf{V}||_2}$ where h^e is the characteristic size of mesh elements.

After FE discretization using the same mesh as in Section 3.1, the PDEs are transformed into a set of coupled nonlinear algebraic equations possessing a sparse tri-band-diagonal structure. This is a distinct advantage over the formulation in [20]. These algebraic equations are solved using a Newton-Raphson procedure where the Jacobian matrix is provided analytically. Despite the PDEs possess N distinct solutions (i.e. one for each mode), only one is relevant for the current shape of the domain and is close to the first guess obtained from the previous domain (see next section). If BCs are well set and the manifold parameterization is still valid (see Section 4.2), the Newton-Raphson procedure converges within 2 or 3 iterations. In this study, the convergence criterion *tol* is satisfied when the L^2 norm of the residue is below 10^{-7}. We note that the PDEs to solve remain nonlinear even if the considered mechanical system is linear.

3.3 Domain prediction

Once the solution for the current annular domain is computed, a new annular domain can be predicted, as illustrated in Figure 2(d). Its inner boundary is defined as the previous outer boundary, whereas its outer boundary is determined by applying an energy increment $\Delta\mathcal{E}$ to the previous outer boundary. The new increment $\Delta\mathcal{E}_{d+1}$ is determined so that the SUPG method requires on average a user-specified number (N^*) of iterations. It follows

$$\Delta\mathcal{E}_{d+1} = \left(\frac{N^*}{N_d}\right) \Delta\mathcal{E}_d \tag{19}$$

where N_d is the actual number of iteration require for the previous domain.

Similarly to the first step of the algorithm, Equation (11) can be used to compute the corresponding nodal displacements Δu^n and Δv^n. The solution at each outer-boundary node of the new domain is computed as follows

$$X_i(u^n + \Delta u^n, v^n + \Delta v^n) = X_i(u^n, v^n) + \left.\frac{\partial X_i}{\partial u}\right|^n \Delta u^n + \left.\frac{\partial X_i}{\partial v}\right|^n \Delta v^n, \tag{20}$$

$$Y_i(u^n + \Delta u^n, v^n + \Delta v^n) = Y_i(u^n, v^n) + \left.\frac{\partial Y_i}{\partial u}\right|^n \Delta u^n + \left.\frac{\partial Y_i}{\partial v}\right|^n \Delta v^n, \tag{21}$$

with $i = 1, ..., N;\ i \neq k$. The new annular domain is meshed, and the solution for all internal nodes is approximated using linear interpolation. Eventually, a complete guess for the solution in the new annular domain is obtained, and the mesh-moving technique of Section 3.1 can be applied.

4 Validation of the proposed method using conservative systems

For conservative systems, the "exact" manifolds can be computed using the numerical continuation technique developed in [13]. This technique, which combines shooting and pseudo-arclength continuation, computes periodic solutions of unforced, undamped nonlinear systems for increasing energies. By gathering in phase space all computed periodic orbits, the invariant manifold of the considered NNM can be built and compared to the invariant manifold computed through the proposed FE-based method.

4.1 2DOF system with geometric nonlinearities

The 2DOF system presented in Figure 3 contains quadratic and cubic nonlinearities arising from second-order terms in the stress tensor. It is an interesting example, because it can exhibit both softening and hardening behaviors. This example was previously studied in references [15, 27, 28]. The governing equations are

$$\ddot{\hat{x}}_1 + \omega_1^2 \hat{x}_1 + \frac{\omega_1^2}{2}\left(3\hat{x}_1^2 + \hat{x}_2^2\right) + \omega_2^2 \hat{x}_1 \hat{x}_2 + \frac{\omega_1^2 + \omega_2^2}{2}\hat{x}_1\left(\hat{x}_1^2 + \hat{x}_2^2\right) = 0 \tag{22}$$

$$\ddot{\hat{x}}_2 + \omega_2^2 \hat{x}_2 + \frac{\omega_2^2}{2}\left(3\hat{x}_2^2 + \hat{x}_1^2\right) + \omega_1^2 \hat{x}_1 \hat{x}_2 + \frac{\omega_1^2 + \omega_2^2}{2}\hat{x}_2\left(\hat{x}_1^2 + \hat{x}_2^2\right) = 0 \tag{23}$$

where $\hat{x}_{1,2} = x_{1,2}/l_0$, and l_0 is the spring's natural length l_0. The system is completely parametrized by the two linear eigenfrequencies ω_1^2 and ω_2^2 [39]. They are chosen equal to 1 and 3, respectively.

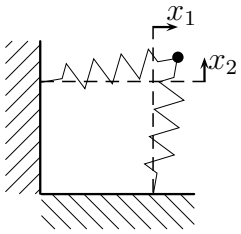

Figure 3: Schematic representation of the 2DOF example.

Figure 4 presents the results for the first NNM of the system. The displacement–velocity pair of the first DOF was considered as master coordinates (u_1, v_1). The invariant manifold corresponding to the constraint relation $X_2(u_1, v_1)$ is presented in phase space in Figure 4(a). Four annular regions were considered for the computation of this manifold, leading to a computational time of 3 minutes in Matlab on a standard laptop computer. The global mesh built from the different annular domains is compared to the reference manifold provided by numerical continuation in Figure 4(b). The two manifolds overlay almost perfectly. In addition, Figure 4(c) shows that a classical Galerkin formulation is associated with spurious element-wise oscillations around the SUPG solution. Interestingly, due to these oscillations, the flow lines can clearly be distinguished. This confirms that the hyperbolic PDEs require specific numerical treatment.

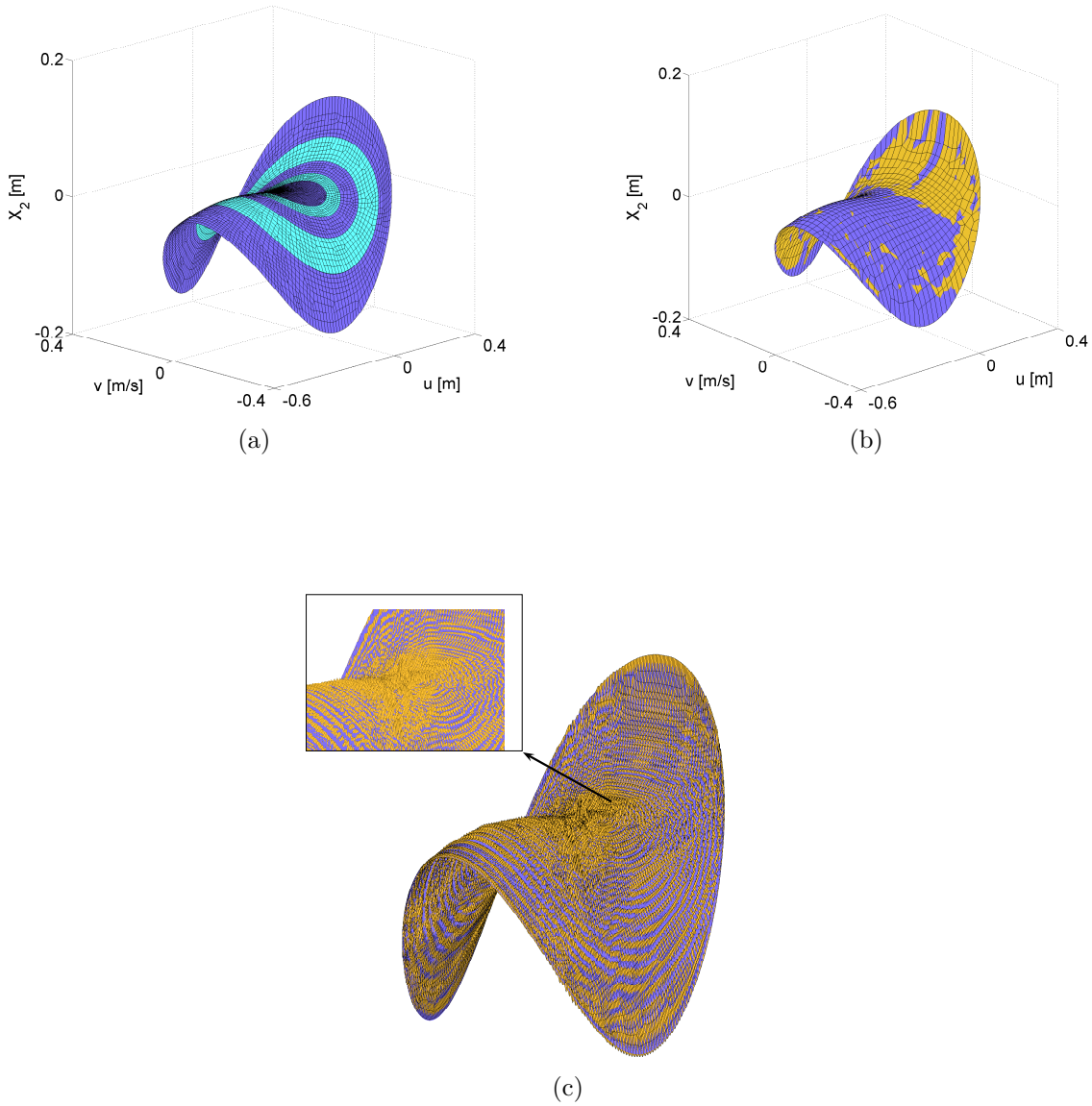

Figure 4: First NNM of the 2DOF system. (a) Invariant manifold X_2 in phase space with the different annular domains; (b) invariant manifold X_2 in phase space (blue: FE method, orange: numerical continuation); (c) Comparison between SUPG (blue) and a classical Galerkin approach (orange).

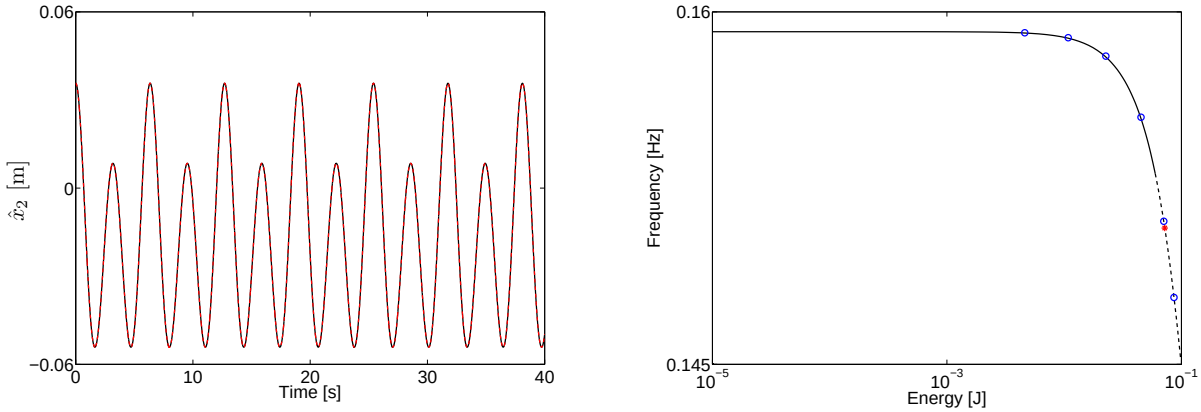

(a) (b)

Figure 5: Validation of the results obtained on the first NNM of the 2DOF system. (a) Comparison between reduced- and full-system dynamics in black and red, respectively; (b) FEP (blue circles: FE method, black solid line: stable branch computed using numerical continuation, black dashed line: unstable branch computed using numerical continuation).

Further validation can be achieved by investigating the nonlinear modal dynamics, i.e., the system dynamics on the manifold. Initial conditions (ICs) on the first mode in modal space (u_1, v_1) corresponding to the red marker in Figure 5(b) are considered, and Equations (5) are integrated over time using a fourth-order Runge-Kutta method. The modal time series are then projected back to the physical space using Equations (3). The ICs are also transformed back to physical space, and a second time integration of the full system's equations (1) is performed considering these ICs. The resulting time series for $\hat{x}_2(t)$ are displayed in Figure 5(a) and agree to the point where the difference between the signals is not visible. The presence of an important second harmonic component in the time series is the sign of a strongly nonlinear regime of motion. A more quantitative comparison is achieved using the normalized mean-square error (NMSE), which is $10^{-7}\%$ in this case.

Due to the frequency-energy dependence of nonlinear oscillations, an appropriate graphical depiction of NNMs is a frequency-energy plot (FEP) in which the NNM frequency is represented at different energy levels [10, 11]. However, because the invariant manifold approach is geometric by nature, the frequency is not a direct by-product of the method. The approach followed here is to estimate, for each iso-energy curve, the NNM period as the sum over each boundary edge of the ratio between the edge length and the norm of the velocity vector $\mathbf{V}$ along the edge. Figure 5(b) presents the FEP of the first NNM as computed by the FE method and by numerical continuation [13]. Blue circles discretize the frequency-energy curve according to the energy increments performed by the FE algorithm while growing the manifold. The softening behavior of the first NNM is perfectly well reproduced by the FE method. Another observation is that the FE method provides accurate results, even for unstable regimes of motion.

The convergence of the FE method is now demonstrated on this first mode. The manifold is computed for different meshes of the same global domain Ω. The domain corresponds to

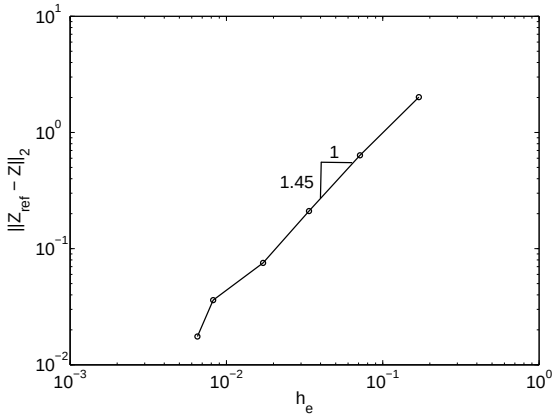

Figure 6: Convergence of the SUPG method.

an iso-energy boundary in order to remove the influence of the mesh-moving technique. As no exact analytical solution exists, a solution $\mathbf{Z}$ is compared to the solution $\mathbf{Z}^{\text{ref}}$ obtained with the finest mesh. Because the different meshes have no common nodes, a direct L^2 measure of the solution error cannot be used. Instead, non-overlapping regions are ignored, and a simple Euclidean vector norm ($||.||_2$) is employed. The convergence rate in Figure 6 is clearly observed for decreasing element characteristic sizes h_e and is close to the theoretically expected value of $O(h_e^{3/2})$ [40].

The results for the second NNM are presented in Figure 7. As for the first NNM, the invariant manifold and FEP computed by the FE and continuation methods overlay very well. Figure 8 compares the dynamics of the slave velocity y_1 reduced on the invariant manifold with the full-system dynamics for the points corresponding to the two red markers in Figure 7(b). In Figure 8(a), there is a good correspondence between both time series; the NMSE is $3.10^{-2}\%$. However, a slight discrepancy is observed for values of y_1 around 0, which is due to a too coarse mesh for small displacements. Decreasing the characteristic size h_e from 0.0198 in Figure 8(a) to 0.0149 in Figure 8(b) resolves this issue; the NMSE reduces to $4.10^{-4}\%$. Figure 8(c) performs the same comparison for initial conditions in the unstable region. Despite the unstable character of the dynamics, both time series match over more than 8 periods and then drift apart. The finer mesh considered in Figure 8(d) can delay this drift.

To conclude the study of this conservative 2DOF system, the first NNM is computed for alternative parameters, $(\omega_1^2, \omega_2^2) = (1.7, 6)$. Figure 9 shows that the system has first a hardening behavior, which is then transformed into softening behavior as energy increases. This interesting dynamics is accurately reproduced by our method.

4.2 Cantilever beam with nonlinear boundary conditions

The algorithm is now validated using a higher-dimensional system, an undamped, cantilever steel beam with nonlinear boundary conditions (see Figure 10). The beam is discretized using 10 linear beam elements resulting in a system of 20 second-order ODEs.

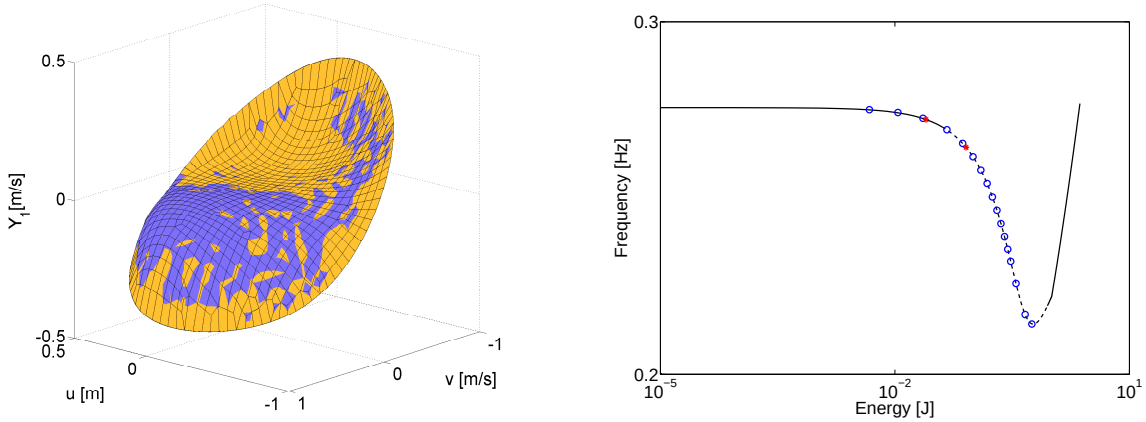

(a) (b)

Figure 7: Second NNM of the 2DOF system. (a) Invariant manifold Y_1 in phase space (blue: FE method, orange: numerical continuation); (b) FEP (blue circles: FE method, black solid line: stable branch computed using numerical continuation, black dashed line: unstable branch computed using numerical continuation)

The 38 unknown, coupled PDEs are solved by considering the displacement and velocity of the first beam element as master coordinates. Figure 11(a) represents the invariant manifold of the second NNM for the constraint relation $Y_8(u_1, v_1)$. Overall, this represents a very large problem with 334400 nodal unknowns (38 $\times$ 8800 nodes). However, thanks to the partition in annular domains, only ten minutes were needed for the computation of the first eight domains. Due to the folding of the manifold at higher energies, it took 20 minutes for the last two annular domains. As confirmed in Figure 11(b), the manifold computed by the FE method is in excellent agreement with that computed using numerical continuation. Figure 12(a) compares the reduced and full-system dynamics for the point depicted by a red marker in Figure 12(b); the NMSE is $10^{-2}\%$. One notes the presence of a very strong third harmonic component, which is the sign of a strongly nonlinear regime of motion. Numerical experimentations demonstrated that, as the number of degrees of freedom of the mechanical system increases, the most effective approach is to use small annular domains combined to a small number of finite elements. However, a sufficient number of element is required to allow convergence up to the desired accuracy *tol*.

Figure 11(c) depicts the invariant manifold computed for larger energies using numerical continuation. The manifold starts to fold and appears to intersect itself but this can be explained by the fact that it is embedded in the full phase space. As mentioned in [19, 24, 25, 27], this folding often arises when a nonlinear coupling, i.e., an internal resonance, between two NNMs exists, but it can also occur in the presence of localization or multiple fixed points. The FEP of Figure 12(b) shows that a tongue of internal resonance indeed appears for high energies. This highlights one intrinsic limitation of the two-dimensional explicit parametrization of the dynamics, which cannot deal with folding of the manifolds. However, as shown in Figure 11(c), our method managed to get very close to this theoretical limit. To circumvent this issue, Shaw and Pierre introduced multi-modal

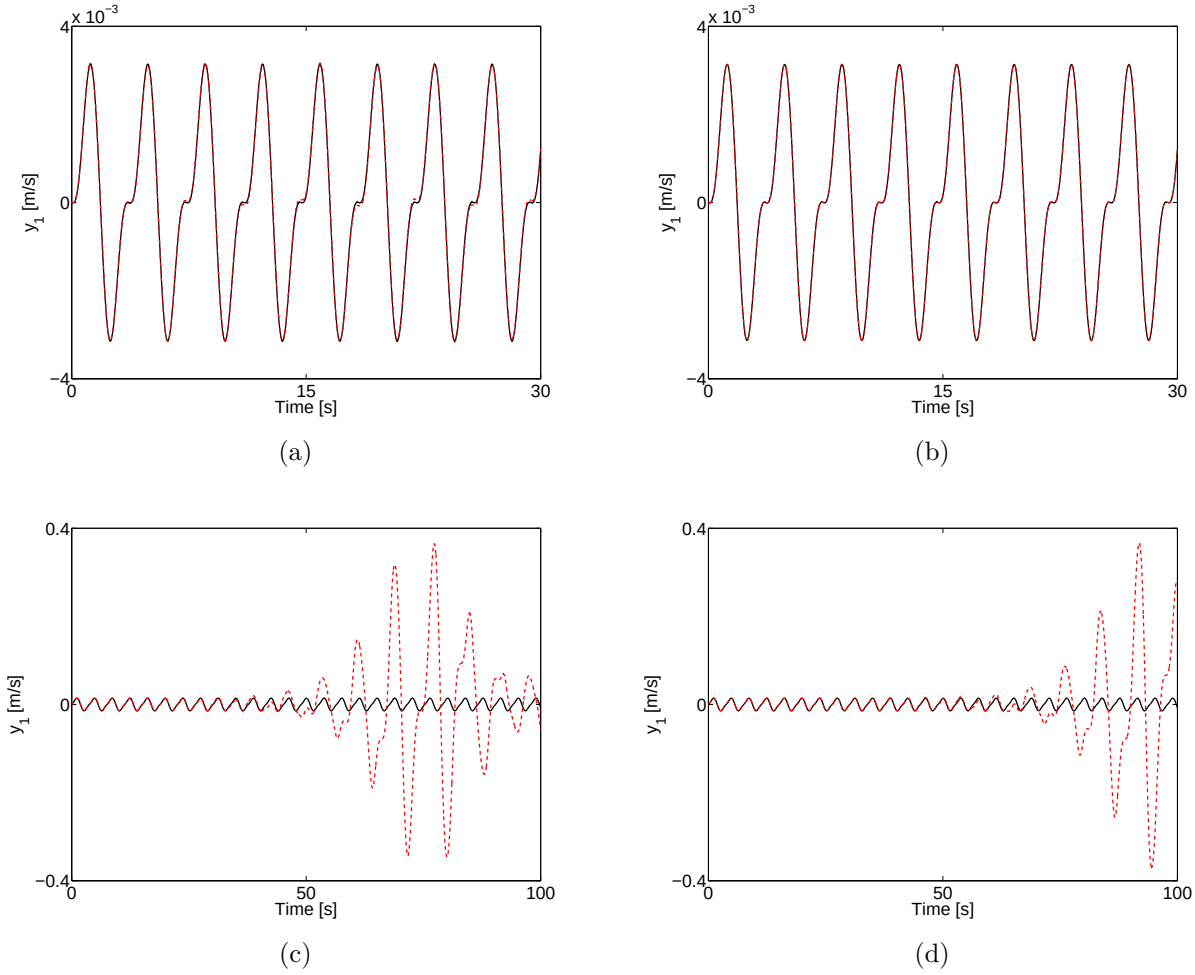

Figure 8: Second NNM of the 2DOF system: comparison between reduced- and full-system dynamics in black and red, respectively. (a, b) Initial conditions in the stable region with $h_e = 0.0198$ and $h_e = 0.0149$, respectively; (c, d) Initial conditions in the unstable region with $h_e = 0.0198$ and $h_e = 0.0149$, respectively.

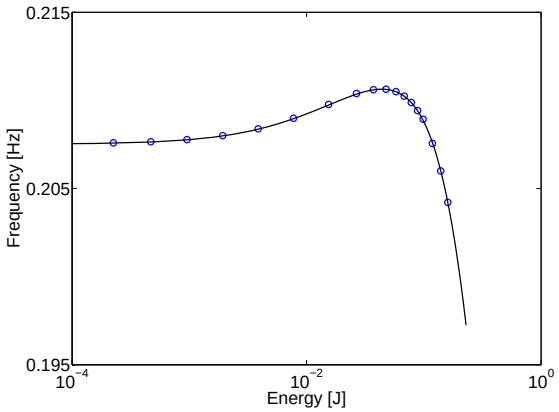

Figure 9: FEP of the first NNM of the 2DOF system for $(\omega_1^2, \omega_2^2) = (1.7, 6)$. Blue circles: FE method, black line: numerical continuation.

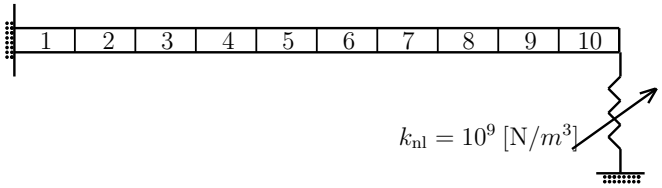

Figure 10: Nonlinear beam: length = 0.7 $[m]$, width = 0.014 $[m]$, height = 0.014 $[m]$.

NNMs where the invariant manifold is described by multiple pairs of master variables [19, 24, 25]. This generalization is not considered in the present study. Note that all the results presented in this paper are computed up to the limits of the parameterization.

5 Extension to nonconservative systems

5.1 Reversing the flow

All the previous developments and results considered the conservative case. This section aims to show that the method can be naturally extended to nonconservative systems. Figure 13 presents the flow field of a 2DOF nonconservative system where, generally speaking, the flow spirals down to the equilibrium point of the system. Unlike the conservative case, the flow now crosses the iso-energetic boundaries, which means that BCs are required at the outer, yet unknown, boundary. A graphical depiction is provided in Figure 14(a).

Mathematically, the flow can be "reversed" by changing the sign of the test functions. Doing so, inflow/outflow boundaries are swapped, as illustrated in Figure 14(b). There is now inflow at the inner boundary. Because the solution in the previous annular domain is available, BCs can be easily imposed at this boundary for solving the PDEs in the current annular domain. As a consequence, the recursive strategy validated for conservative

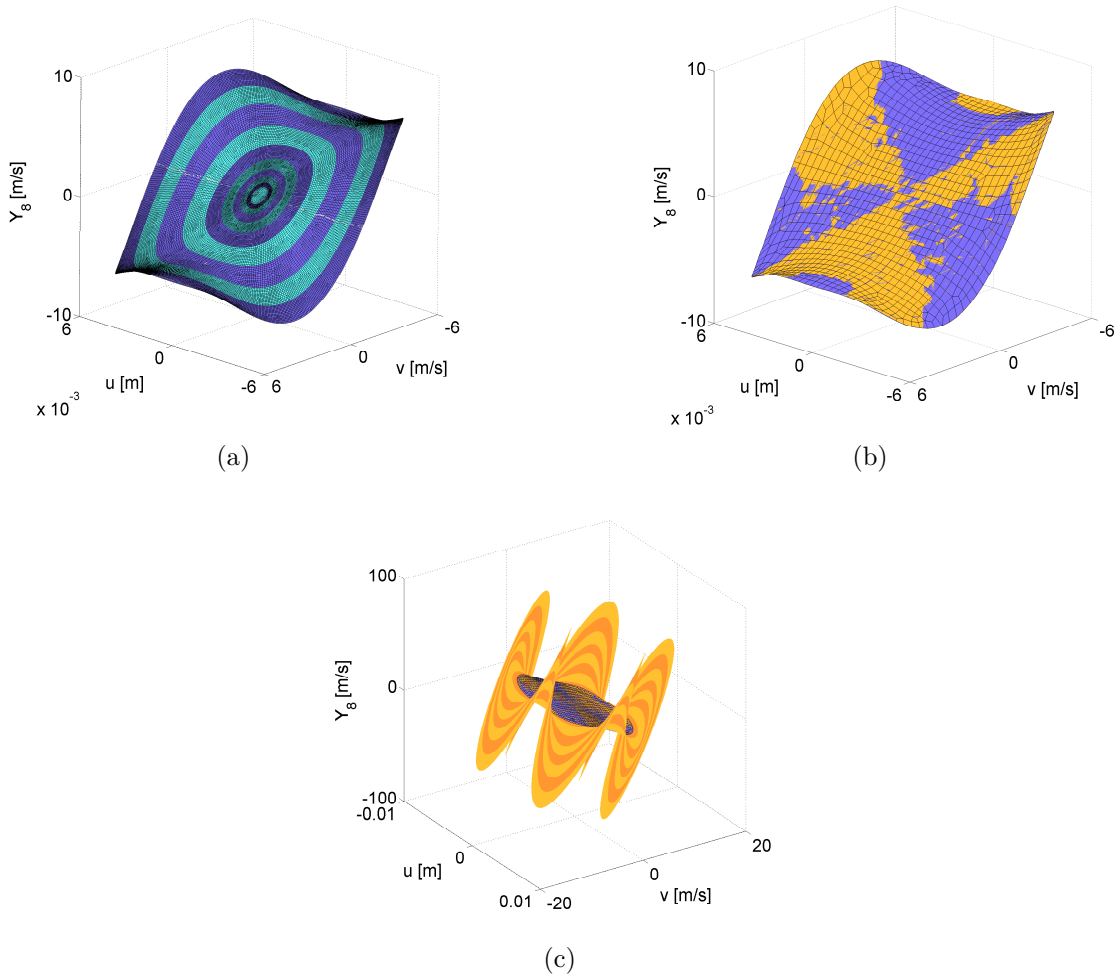

Figure 11: Second bending mode of the beam. (a) Invariant manifold Y_8 in phase space with the different annular domains; (b) Invariant manifold Y_8 in phase space (blue: FE method, orange: numerical continuation). For clarity, only 1212 nodes out of the 8800 used for the computation are represented. (c) Invariant manifold computed for larger energies (blue: FE method, orange: numerical continuation).

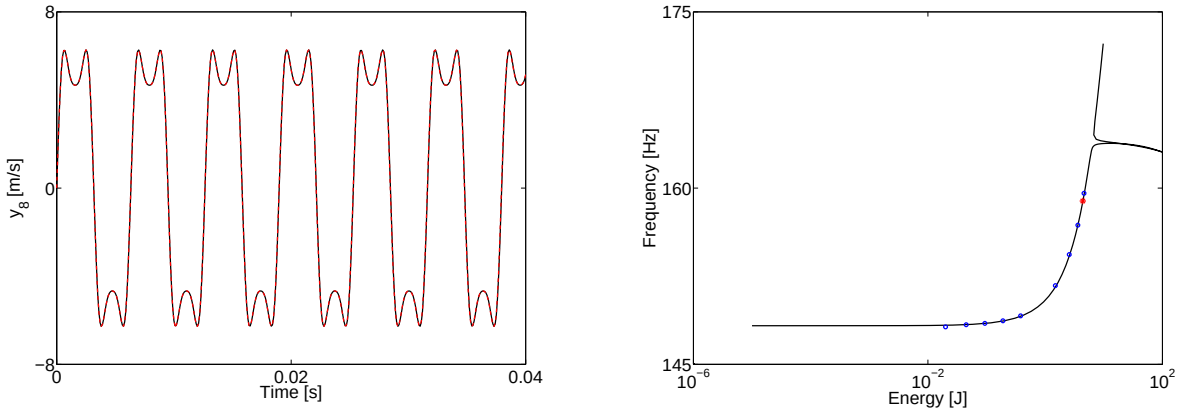

(a) (b)

Figure 12: Second bending mode of the beam. (a) Comparison between reduced- and full-system dynamics in black and red, respectively; (b) FEP (blue circles: FE method, black line: numerical continuation).

systems can be applied as such in the nonconservative case.

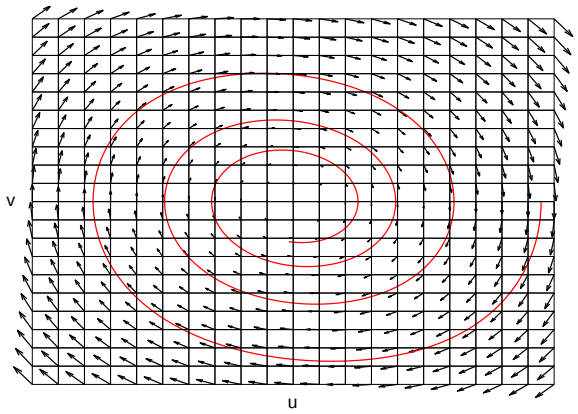

Figure 13: Trajectory (−) and velocity vector $\mathbf{V}$ (→) of the manifold-governing PDEs for a 2DOF nonconservative system.

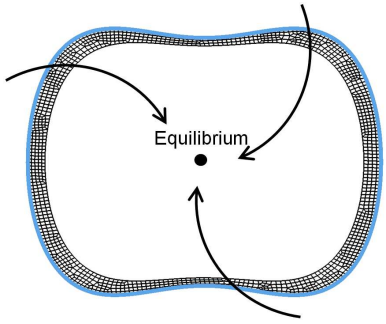

(a)

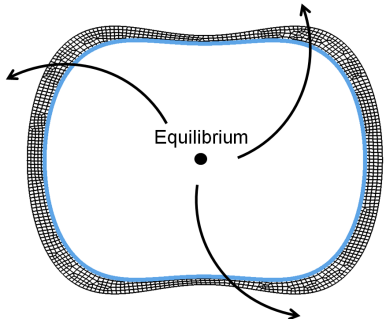

(b)

Figure 14: Schematics of the extension of the algorithm to nonconservative systems. BCs are required at the inflow boundary $\partial\Omega^-$ depicted in light blue. (a) Original problem; (b) Problem with reversed flow.

5.2 2DOF system with geometric nonlinearities

The 2DOF example studied in Section 4 is considered with linear damping

$$\begin{aligned}\ddot{\hat{x}}_1 + 2\omega_1\zeta_1\dot{\hat{x}}_1 + \omega_1^2\hat{x}_1 + \frac{\omega_1^2}{2}\left(3\hat{x}_1^2 + \hat{x}_2^2\right) \\ + \omega_2^2\hat{x}_1\hat{x}_2 + \frac{\omega_1^2+\omega_2^2}{2}\hat{x}_1\left(\hat{x}_1^2 + \hat{x}_2^2\right) = 0 \\ \ddot{\hat{x}}_2 + 2\omega_2\zeta_2\dot{\hat{x}}_2 + \omega_2^2\hat{x}_2 + \frac{\omega_2^2}{2}\left(3\hat{x}_2^2 + \hat{x}_1^2\right) \\ + \omega_1^2\hat{x}_1\hat{x}_2 + \frac{\omega_1^2+\omega_2^2}{2}\hat{x}_2\left(\hat{x}_1^2 + \hat{x}_2^2\right) = 0 \quad (24)\end{aligned}$$

where $(\omega_1^2, \omega_2^2) = (1.8, 6)$. Figure 15(a,b) presents the system's frequency response to harmonic excitation computed for different forcing amplitudes and damping values. The computations are carried out using a numerical continuation algorithm [41]. For $(\zeta_1, \zeta_2) = (0.001, 0.005)$, a clear hardening behavior is observed, whereas softening behavior is present for $(\zeta_1, \zeta_2) = (0.001, 0.2)$. It is interesting that "simple" viscous damping can lead to such fundamental changes in the dynamics [15].

Because nonlinear resonances occur in the neighborhood of NNMs [2], this behavior can also be predicted by the damped NNMs. The manifolds computed for the two damping values are presented in Figure 16. In the presence of weak damping, the invariant manifold in Figure 16(a) possesses the same characteristic shape as for the conservative system (Figure 4). However, strong damping dramatically modifies its structure as illustrated in Figure 16(b). The backbone curves shown in dashed lines in Figure 15(a,b) were computed by integrating in time the dynamics on the computed manifolds and by extracting the frequency-amplitude dependence from the free-decay response. The computed backbones are in perfect agreement with the results given by numerical continuation, which validates the proposed algorithm in the damped case.

5.3 Cantilever beam with nonlinear boundary conditions

Proportional damping with $\mathbf{C} = \alpha\mathbf{M} + \beta\mathbf{K}$ where $\alpha = 5$ and $\beta = 5e-6$ is introduced in the cantilever beam example. The (linear) damping ratio for the first mode is 0.7%. The slave velocity Y_{19} obtained for this damped system is displayed in Figure 17(a). In the presence of damping, no reference manifold computed using a well-established method exists, and results validation relies on time integration. Figure 17(b) compares the reduced and full dynamics. They agree very well with an NMSE value of 7.10^{-3}%. Figure 17(c) examinates the invariant manifold computed for the undamped (blue) and littly damped (orange) cases. First, both surfaces appear identical. It is explained by the proportional character of the damping which does not modify the LNM underlying the NNM. Only the dynamics on the invariant manifold is modified whereas its geometry is unchanged. Second, it appears that the presence of damping has slightly shorten the region where the manifold parameterization is valid. The manifold was therefore computed for smaller values.

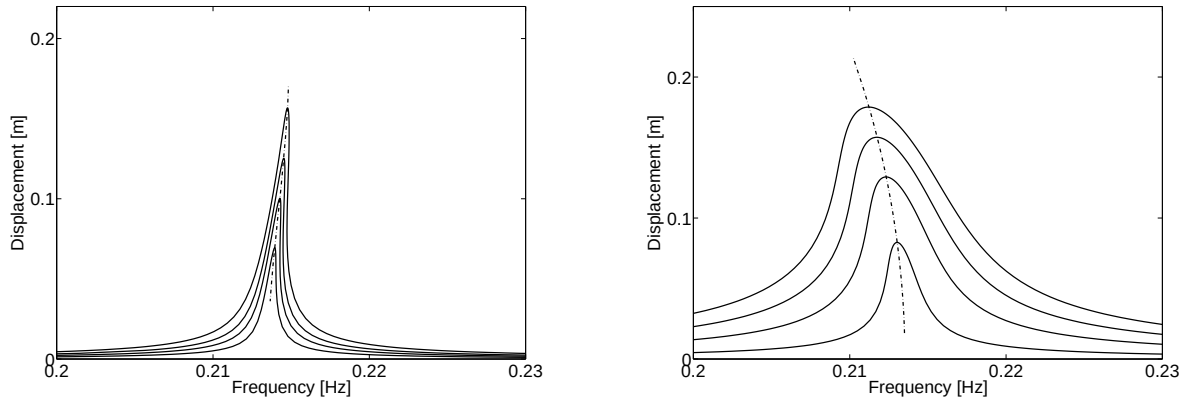

(a) (b)

Figure 15: Frequency response of the damped 2DOF system to harmonic forcing. (a) $(\zeta_1, \zeta_2) = (0.001, 0.005)$; (b) $(\zeta_1, \zeta_2) = (0.001, 0.2)$. Solid line: numerical continuation; dashed line; backbone curves extracted from damped NNMs.

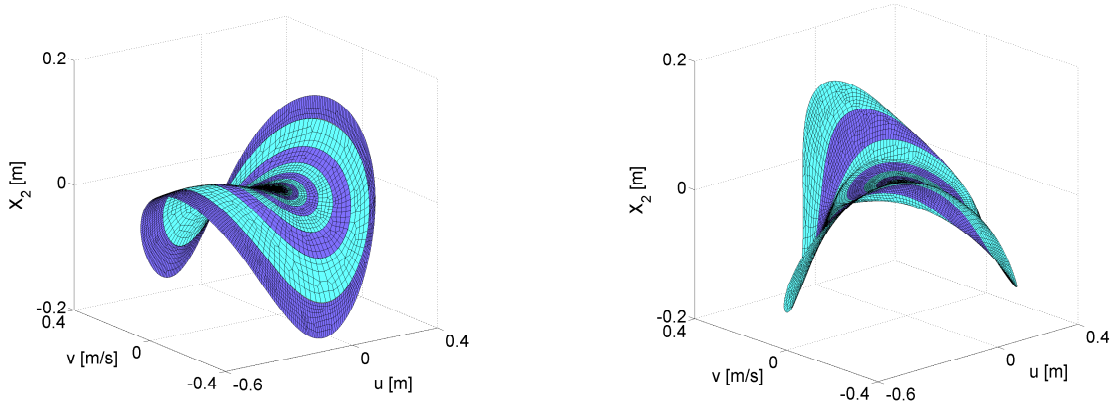

(a) (b)

Figure 16: Annular domains computed for the first NNM of the damped 2DOF system. (a) $(\zeta_1, \zeta_2) = (0.001, 0.005)$; (b) $(\zeta_1, \zeta_2) = (0.001, 0.2)$.

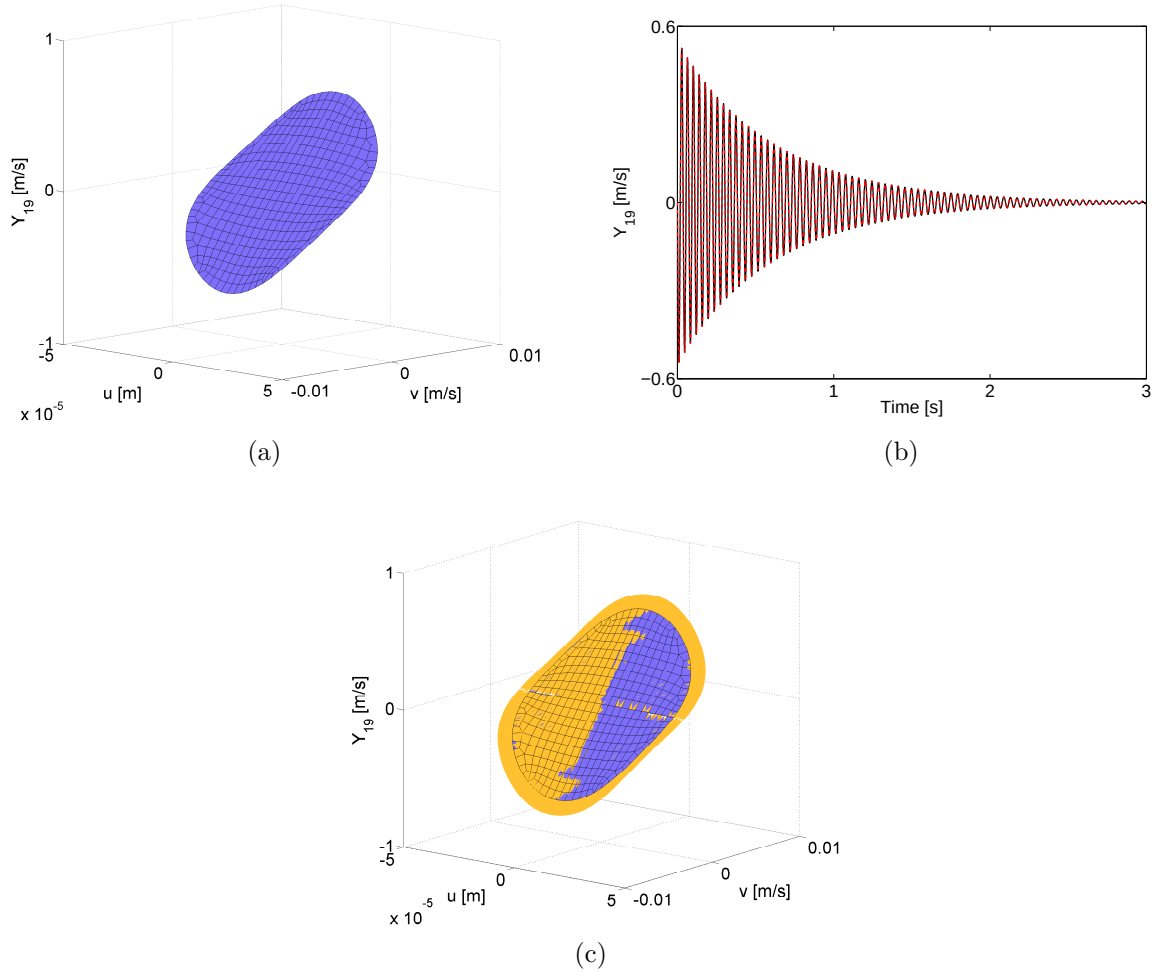

Figure 17: First NNM of the nonconservative beam. (a) Invariant manifold Y_{19}. (b) Comparison between reduced- and full-system dynamics in black and red, respectively. (c) Comparison between the invariant manifold Y_{19} for the damped (blue) and undamped (orange) systems.

6 Conclusions

In this paper, a new computational method is introduced for calculating the NNMs of nonlinear mechanical structures. The approach targets the computation of two-dimensional undamped and damped invariant manifolds and solves the manifold-governing PDEs using the FE method. Specifically, the SUPG method combined with an annular resolution strategy are used for addressing the hyperbolic nature of the PDEs and the high computational burden. As a result, the method is computationally effective even for systems with relatively high dimensionality. Another advantage is that it is not restricted to small-amplitude motions. One limitation of the method that is inherent to the two-dimensional parametrization of the manifold is that it cannot handle internal resonances between the modes.

Acknowledgements

The author L. Renson would like to acknowledge the Belgian National Fund for Scientific Research (FRIA fellowship) for its financial support.

References

[1] R. M. Rosenberg. On nonlinear vibrations of systems with many degrees of freedom. *Advances in Applied Mechanics*, Volume 9:155–242, 1966.

[2] A. F. Vakakis, L. I. Manevitch, Y V. Mlkhlin, V. N. Pilipchuk, and A. A. Zevin. *Normal Modes and Localization in Nonlinear Systems*. Wiley-VCH Verlag GmbH, 2008.

[3] S. W. Shaw and C. Pierre. Normal modes for non-linear vibratory systems. *Journal of Sound and Vibration*, 164:40, 1993.

[4] A. F. Vakakis. Non-linear normal modes (NNMs) and their applications in vibration theory: An overview. *Mechanical Systems and Signal Processing*, 11(1):3–22, 1997.

[5] L. Jezequel and C. H. Lamarque. Analysis of non-linear dynamical systems by the normal form theory. *Journal of Sound and Vibration*, 149(3):429–459, 1991.

[6] W. Lacarbonara and R. Camillacci. Nonlinear normal modes of structural systems via asymptotic approach. *International Journal of Solids and Structures*, 41(20):5565–5594, 2004.

[7] O. V. Gendelman. Bifurcations of nonlinear normal modes of linear oscillator with strongly nonlinear damped attachment. *Nonlinear Dynamics*, 37(2):115–128, 2004.

[8] S. Lenci and G. Rega. Dimension reduction of homoclinic orbits of buckled beams via the non-linear normal modes technique. *International Journal of Non-Linear Mechanics*, 42(3):515–528, 2007.

[9] J. Warminski. Nonlinear normal modes of a self-excited system driven by parametric and external excitations. *Nonlinear Dynamics*, 61(4):677–689, 2010.

[10] Y. S. Lee, G. Kerschen, A. F. Vakakis, P. Panagopoulos, L. Bergman, and D. M. McFarland. Complicated dynamics of a linear oscillator with a light, essentially nonlinear attachment. *Physica D: Nonlinear Phenomena*, 204(1-2):41–69, 2005.

[11] G. Kerschen, M. Peeters, J. C. Golinval, and A. F. Vakakis. Nonlinear normal modes, part I: A useful framework for the structural dynamicist. *Mechanical Systems and Signal Processing*, 23(1):170–194, 2009.

[12] R. Arquier, S. Bellizzi, R. Bouc, and B. Cochelin. Two methods for the computation of nonlinear modes of vibrating systems at large amplitudes. *Computers & Structures*, 84(24-25):1565–1576, 2006.

[13] M. Peeters, R. Viguié, G. Sérandour, G. Kerschen, and J. C. Golinval. Nonlinear normal modes, part II: Toward a practical computation using numerical continuation techniques. *Mechanical Systems and Signal Processing*, 23(1):195–216, 2009.

[14] G. Kerschen, M. Peeters, J.C. Golinval, and C. Stephan. Nonlinear normal modes of a full-scale aircraft. *AIAA Journal of Aircraft, in press*, in press, 2013.

[15] C. Touzé and M. Amabili. Nonlinear normal modes for damped geometrically nonlinear systems: Application to reduced-order modelling of harmonically forced structures. *Journal of Sound and Vibration*, 298(4-5):958–981, 2006.

[16] N. Boivin, C. Pierre, and S. W. Shaw. Nonlinear normal modes, invariance, and modal dynamics approximations of nonlinear systems. *Nonlinear Dynamics*, 8:32, 1995.

[17] S.-L. Chen and S. W. Shaw. Normal modes for piecewise linear vibratory systems. *Nonlinear Dynamics*, 10:135–164, 1996.

[18] N. Boivin, C. Pierre, and S. W. Shaw. Non-linear modal analysis of the forced response of structural systems. *AIAA Journal*, page 22, 1996.

[19] N. Boivin, C. Pierre, and S. W. Shaw. Non-linear modal analysis of structural systems featuring internal resonances. *Journal of Sound and Vibration*, 182:6, 1995.

[20] E. Pesheck, C. Pierre, and S. W. Shaw. A new Galerkin-based approach for accurate non-linear normal modes through invariant manifolds. *Journal of Sound and Vibration*, 249(5):971–993, 2002.

[21] E. Pesheck. *Reduced order modeling of nonlinear structural systems using nonlinear normal modes and invariant manifolds*. PhD thesis, University of Michigan, 2000.

[22] D. Jiang, C. Pierre, and S. W. Shaw. Large-amplitude non-linear normal modes of piecewise linear systems. *Journal of Sound and Vibration*, 272(3-5):869–891, 2004.

[23] D. Jiang, C. Pierre, and S. W. Shaw. Nonlinear normal modes for vibratory systems under harmonic excitation. *Journal of Sound and Vibration*, 288(4-5):791–812, 2005.

[24] E. Pesheck, N. Boivin, C. Pierre, and S. W. Shaw. Nonlinear modal analysis of structural systems using multi-mode invariant manifolds. *Nonlinear Dynamics*, 25, 2001.

[25] D. Jiang, C. Pierre, and S. W. Shaw. The construction of non-linear normal modes for systems with internal resonance. *International Journal of Non-Linear Mechanics*, 40(5):729–746, 2005.

[26] M. Legrand, D. Jiang, C. Pierre, and S. W. Shaw. Nonlinear normal modes of a rotating shaft based on the invariant manifold method. *International Journal of Rotating Machinery*, 10(4):319–335, 2004.

[27] F. Blanc, C. Touzé, J. F. Mercier, K. Ege, and A. S. Bonnet Ben-Dhia. On the numerical computation of nonlinear normal modes for reduced-order modelling of conservative vibratory systems. *Mechanical Systems and Signal Processing*, 36(2):520–539, 2013.

[28] S. Bellizzi and R. Bouc. A new formulation for the existence and calculation of nonlinear normal modes. *Journal of Sound and Vibration*, 287(3):545–569, 2005.

[29] S. Bellizzi and R. Bouc. An amplitude-phase formulation for nonlinear modes and limit cycles through invariant manifolds. *Journal of Sound and Vibration*, 300(3-5):896–915, 2007.

[30] D. Laxalde and F. Thouverez. Complex non-linear modal analysis for mechanical systems: Application to turbomachinery bladings with friction interfaces. *Journal of Sound and Vibration*, 322(4−5):1009–1025, 2009.

[31] S. Larsson and V. Thomée. *Partial Differential Equations with Numerical Methods*, volume 45. Springer Berlin Heidelberg, 2003.

[32] M. Renardy and R. Rogers. *An Introduction to Partial Differential Equations*, volume 13. Springer Berlin Heidelberg, 2004.

[33] K. Stein, T. E. Tezduyar, and R. Benney. Automatic mesh update with the solid-extension mesh moving technique. *Computer Methods in Applied Mechanics and Engineering*, 193(21-22):2019–2032, 2004.

[34] Z. Xu and M. Accorsi. Finite element mesh update methods for fluid-structure interaction simulations. *Finite Elements in Analysis and Design*, 40(9-10):1259–1269, 2004.

[35] A. Ern and J.-L. Guermond. *Theory and Practice of Finite Elements*, volume 159 of *Applied Mathematical Sciences*. Springer New York, 2004.

[36] J. Donea and A. Huerta. *Steady Transport Problems*. Finite Element Methods for Flow Problems. John Wiley & Sons, Ltd, 2005.

[37] A. N. Brooks and T. J. R. Hughes. Streamline upwind/Petrov-Galerkin formulations for convection dominated flows with particular emphasis on the incompressible Navier-Stokes equations. *Computer Methods in Applied Mechanics and Engineering*, 32(1-3):199–259, 1982.

[38] T. J. R. Hughes and T. E. Tezduyar. Finite element methods for first-order hyperbolic systems with particular emphasis on the compressible Euler equations. *Computer Methods in Applied Mechanics and Engineering*, 45(1-3):217–284, 1984.

[39] C. Touzé, O. Thomas, and A. Huberdeau. Asymptotic non-linear normal modes for large-amplitude vibrations of continuous structures. *Computers & Structures*, 82(31-32):2671–2682, 2004.

[40] C. Johnson, U. Nävert, and J. Pitkäranta. Finite element methods for linear hyperbolic problems. *Computer Methods in Applied Mechanics and Engineering*, 45(1-3):285–312, 1984.

[41] R. Seydel. *Practical Bifurcation and Stability Analysis*, volume 5 of *Interdisciplinary Applied Mathematics*. Springer New York, 2010.